GFZ

Helmholtz-Zentrum
POTSDAM

Originally published as:

High-resolution local earthquake tomography of the southern Dead Sea area

B. Braeuer,[1] Guenter Asch,[1] R. Hofstetter,[2] Ch. Haberland,[1] D. Jaser,[3] R. El-Kelani[4] and M. Weber[1,5]

[1]*Deutsches GeoForschungsZentrum Potsdam (GFZ), Telegrafenberg,* 14473 *Potsdam, Germany. E-mail: ben@gfz-potsdam.de*
[2]*Geophysical Institute of Israel (GII), PO Box* 182, *Lod* 71100, *Israel*
[3]*Natural Resources Authority (NRA), Eight circle, PO Box* 7, *Amman, Jordan*
[4]*An-Najah National University, PO Box* 7, *Nablus, West Bank, Palestine*
[5]*Institute of Earth and Environmental Science, Karl-Liebknecht-Str.* 24-25, 14476 *Potsdam, University of Potsdam, Germany*

GJI Geodynamics and tectonics

SUMMARY

Local earthquake data from a dense temporary seismological network in the southern Dead Sea area have been analysed within the project DESIRE (Dead Sea Integrated Research Project). Local earthquakes are used for the first precise image of the distribution of the *P*-wave velocity and the v_P/v_S ratios. 65 stations registered 655 local events within 18 months of observation time. A subset of 530 well-locatable events with 26 730 *P*- and *S*-arrival times was used to calculate a tomographic model for the v_P and v_P/v_S distribution. Since the study area is at first-order 2-D, a gradual approach was chosen, which compromised a 2-D inversion followed by a 3-D inversion. The sedimentary basin fill is clearly imaged through high v_P/v_S ratios and low v_P. The basin fill shows an asymmetric structure with average depth of 7 km at the western boundary and depth between 10 and 14 km at the eastern boundary. This asymmetry is reflected by the vertical strike-slip eastern border fault, and the normal faulting at the western boundary, caused by the transtensional deformation within the last 5 Myr. Within the basin fill the Lisan salt diapir is imaged through low v_P/v_S ratios, reflecting its low fluid content. The extensions were determined to 12 km in E–W and 17 km in N–S direction while its depth is 5–6 km. The thickness of the pre-basin sediments below the basin fill cannot be derived from the tomography data—it is estimated to less than 3 km from former investigations. Below the basin, down to 18 km depth very low *P*-wave velocities and low v_P/v_S ratios are observed—most likely caused by fluids from the surrounding crust or the upper mantle.

Key words: Seismic tomography; Continental margins: transform; Continental tectonics: strike-slip and transform.

1 INTRODUCTION

The Dead Sea transform (DST) Fault is one of the largest transform faults in the world extending over 1000 km from the Red Sea in the south to the Taurus collision zone in the north. It forms the boundary between the Arabian Plate and the African Plate (Fig. 1). The relative left-lateral motion of these two plates, which started in the early Miocene (~18 Myr), caused a total shift of ~107 km (e.g. Quennel 1958; Freund *et al.* 1970). The recent slip rate is estimated from different authors (e.g. Klinger *et al.* 2000; Reilinger *et al.* 2006; Le Beon *et al.* 2008) to be ~4 mm a^{-1}.

One of the prominent features along the DST is the Dead Sea Basin (DSB), a large sedimentary basin filled with clastics and evaporites. It is situated between the Arava valley in the south and the Jordan valley in the north. The left-lateral motion along the

DST is most likely responsible for the development of the DSB, and therefore, most authors agree on the concept of a pull-apart basin for the formation of the DSB (extensive discussion in Garfunkel 1997). The main strike-slip motion side-steps from the east side (Arava Fault) of the valley at the southern end of the basin to the west side (Jericho Fault) of the valley north of the basin (e.g. Garfunkel 1981; ten Brink *et al.* 1993; Gardosh *et al.* 1997). The initiation of the formation of the DSB was 18–15 Myr (Garfunkel 1981; Garfunkel & Ben-Avraham 1996), that is, together with the beginning of the transform motion. The total length of the basin is therewith at least 107 km, that is, consistent with the shift along the DST (e.g. Larsen *et al.* 2002) while it is only 15–17 km wide.

Though the DSB has been studied for a long time, the available knowledge—based mainly on surface geology, drilling and seismic reflection surveys—gives only a partial picture of its shallow
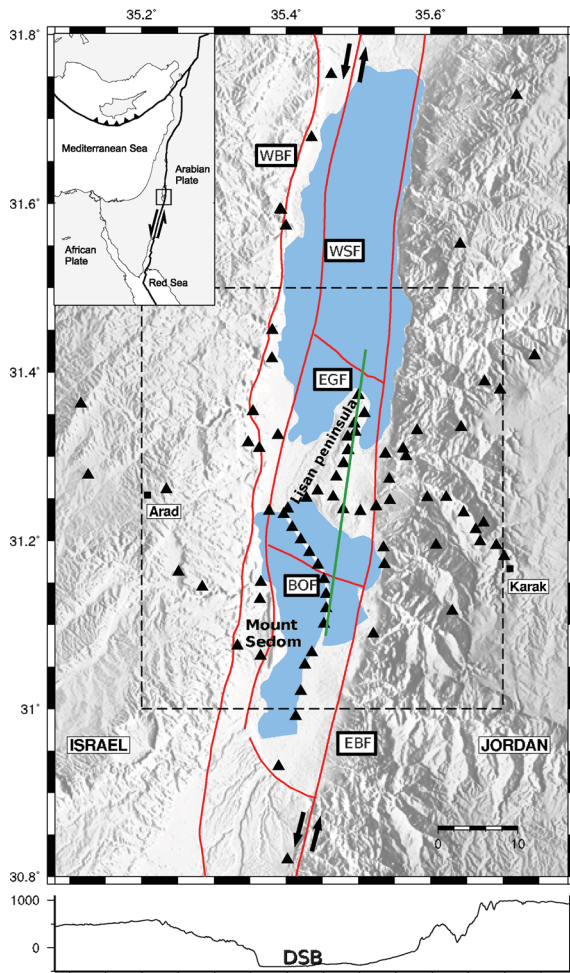
Figure 1. Site map of the DESIRE seismograph network. Used stations of the permanent networks in Israel and Jordan are also indicated. The areas which are covered with water recently are marked in blue: in the north the natural Dead Sea, in the south the evaporation ponds which are filled artificially with water to harvest minerals through evaporation. The dashed box is indicating the area shown for the 3-D model (e.g. Fig. 9). Only the main faults are indicated as solid red lines. Arava Fault or eastern border fault (EBF, strike-slip); Jericho Fault or WSF and western boundary fault (WBF), here collectively called western faults (WF). The two faults bordering the Lisan diapir: Ein Gedi Fault (EGF), Boqeq Fault (BOF). The green line is indicating the NS profile of Fig. 12. On the bottom a topographic profile from west to east at Lat 31.25° is shown.

2 TECTONIC SETTING, GEOLOGY AND SEISMICITY

The structure of the DSB is dominated by longitudinal intrabasinal faults, the extensions of the Arava (eastern boundary fault, EBF) and Jericho (western strike-slip fault, WSF) master faults (Garfunkel 1997; Garfunkel & Ben-Avraham 2001), which accommodate the main left-lateral movement responsible for the basin formation (Fig. 1). It is crossed obliquely by several secondary transverse faults that divide it into different segments with different depths (e.g. Garfunkel & Ben-Avraham 1996). These transverse faults, trending mostly NW–SE obliquely across the basin, are observed in all parts of the basin (e.g. Ben-Avraham & Ten Brink 1989). In our study area, two transverse faults are located: the Boqeq Fault and the Ein Gedi Fault, forming the southern and northern borders of the Lisan diapir below the Lisan Peninsula, respectively (Fig. 1, Ben-Avraham & Ten Brink 1989; Larsen *et al.* 2002).

The DSB is divided into a northern and a southern sub-basin, separated by the Lisan salt diapir below the Lisan Peninsula (see Fig. 1). The salt of the Lisan diapir comes from the Sedom formation, which gets its name from the second diapir in the basin, the Sedom diapir (below Mt Sedom in Fig. 1) in the southwest of the basin. A magnetotelluric profile over the Lisan Peninsula identified the Lisan diapir as a resistive body, that is, composed of dry salt with low porosity (Meqbel *et al.* 2012). The Lisan diapir separates the shallow northern sub-basin (6–8 km deep, Ginzburg & Ben-Avraham 1997) from the deeper southern sub-basin, where the study area is mostly located. From a teleseismic *P*-wave tomography study a sediment thickness larger than 10 km was estimated for the southern DSB (Hofstetter *et al.* 2000) while ten Brink *et al.* (1993) estimated about 16 km from a gravimetrical study. A NS refraction seismic profile (Ginzburg & Ben-Avraham 1997) revealed about 14 km sediment thickness, while a WE refraction seismic profile crossing the Lisan Peninsula revealed only 11 km (Mechie *et al.* 2009). Furthermore, in two WE refraction profiles reduced *P*-wave velocities down to 18 km depth were found (ten Brink *et al.* 2006; Mechie *et al.* 2009).

Some authors point out the asymmetry of the basin in the E–W direction with a deep and nearly vertical EBF and a shallower WBF inclined to the east (Neev & Hall 1979; Zak & Freund 1981; Garfunkel & Ben-Avraham 1996; Garfunkel 1997; Shamir 2006). Ben-Avraham & Zoback (1992) introduced the concept of an asymmetric basin with transform-normal extension in addition to the main left-lateral motion in regions under transtensional regimes (e.g. Marmara Sea, Le Pichon *et al.* 2001). In an asymmetric basin, one of the two boundary faults is approximately vertical and shows a strike-slip movement, while the other boundary fault is flatter and shows primarily transform-normal extension, that is, normal faulting (Ben-Avraham & Zoback 1992).

Thick layers of sediments fill the basin. Clastics and evaporites were deposited during periods of different climate and varying water sources (fresh or salt), which transported the sediments into the basin (Garfunkel & Ben-Avraham 1996). The upper 4 km of the basin fill consists of Pleistocene to Holocene sediments underlain by about 1 km of Pliocene salt. The rest of the originally 2-km-thick salt layer ascended as the Sedom and Lisan salt diapirs (Al-Zoubi & ten Brink 2001). Miocene sediments, the first deposits after the beginning of the basin formation, are found below it with a thickness of up to 4 km (Ben-Avraham & Schubert 2006). The pre-basin sediments of Cretaceous and pre-Cretaceous age, forming the uppermost 3-km-thick layer east and west of the basin (Mechie

structure. Local earthquake tomography (LET; Thurber 1993) is widely used to obtain high-resolution crustal images in seismically active regions and is applied here to shed light on the deeper structure of the sedimentary basin. We thus present the results of a simultaneous inversion of v_P, v_P/v_S ratios and hypocentral parameters based on a 17 month study of local earthquakes in the southern Dead Sea area. The *P* velocity is often characterizing different lithologies and can be thus used to distinguish between sediments and basement rocks. The ratio of *P* and *S* velocity is related to porosity (Marquis & Hyndman 1992; Takei 2002), which is often linked to fluid content. Thus, the v_P/v_S ratio is used to map differences in the fluid content (e.g. Eberhart-Phillips & Bannister 2010). In our study area the ratio can be used, for example, to differentiate between salt and other marine sediments.

et al. 2009), form the lowest layer of the basin fill. Its thickness is estimated from different authors to be 2.5–7 km (ten Brink *et al.* 1993; Ginzburg & Ben-Avraham 1997; Mechie *et al.* 2009).

A seismic refraction profile (Mechie *et al.* 2009) crossing the DSB in W–E direction in the area of the Lisan Peninsula (Fig. 1) suggests only a small variation of the Moho below the DSB, contradicting, for example, Garfunkel (1997), and a boundary between the upper and lower crust at 20 km depth acting as a decoupling zone. Thus, the DSB does not follow the classical behaviour of sedimentary basins with crustal thinning related to the amount of subsidence due to the requirement of isostatic equilibrium (ten Brink *et al.* 1993). Instead, it seems to be an upper crustal feature with small to no effects of crustal thinning and mantle upwelling (ten Brink *et al.* 2006; Mechie *et al.* 2009).

Instrumental recording of earthquakes in the Dead Sea area started at the beginning of the last century. Beginning in 1984 a permanent seismic network was installed in Israel, which enabled to monitor the microseismic activity at the DST, showing remarkable activity in the DSB. However, as the distance of adjacent stations within the network is larger than 20 km, only events with magnitudes smaller than 2 can be registered. With additional stations from a temporary network van Eck & Hofstetter (1989) were able to make first estimations of the microseismicity distribution. The eastern boundary of the basin is active only in the south, while in the north activity at both boundaries was found.

Aldersons *et al.* (2003) used for their analysis stations from Israel and Jordan and were thus able to determine the depth distribution of the events. Most of the earthquakes nucleated between 20 and 32 km depth, thus in the lower crust, while the upper mantle appears to be aseismic for the 14 yr observation period.

3 DATA ACQUISITION

For the study presented here, between 2006 October and 2008 March a dense seismic network consisting of 65 stations was deployed in the Dead Sea region, with emphasis on the south, covering the DSB as well as the shoulders east and west of it (Fig. 1).

The average spacing (distance to the first neighbour) was 2.5 km in Jordan and 4.5 km in Israel. The stations in the basin were located 300 m below mean sea level (Fig. 1). At the shoulders of the basin the highest station was located at an elevation of 614 m (Israel—west) and 1096 m (Jordan—east), respectively. About 1–2 local events per day were recorded. All stations were equipped with Earth Data Loggers (EDL) as recording units. 38 of our stations were equipped with Mark L-4C-3D short period sensors. The other 27 recorders were equipped with GURALP CMG-40T or CMG-3T, or with STS-2 seismometers. Unfortunately we encountered problems with vandalism and theft in some locations in Israel leading to loss of some stations and the necessity for redeployment of some others in 2008 June, enlarging the study area to the north and to the south (see Fig. 1).

Event detection was done manually due to the expected large number of events with very low magnitude, i.e. with low signal-to-noise ratio. Determination of accurate arrival times and initial locations was done manually with the software JSTAR provided by the Geophysical Institute of Israel (GII). The arrival time determination was done on unfiltered raw data, whenever possible. The waveform example in Fig. 2 shows that the *S*-wave onsets were generally more impulsive than the *P*-wave onsets, resulting in an unusually high number of *S*-wave traveltime picks. The *S*-wave onsets were picked only from horizontal components, also to avoid picking of *S* precursors from expected *P*-to-*S* conversions on the
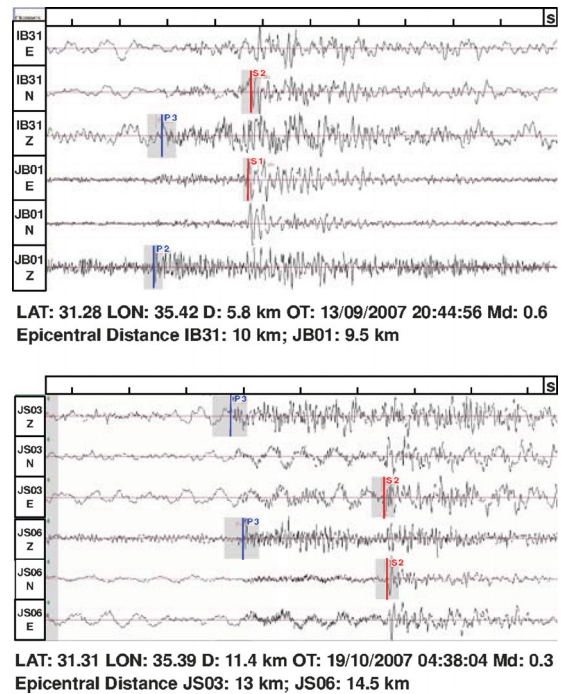

LAT: 31.28 LON: 35.42 D: 5.8 km OT: 13/09/2007 20:44:56 Md: 0.6
Epicentral Distance IB31: 10 km; JB01: 9.5 km

LAT: 31.31 LON: 35.39 D: 11.4 km OT: 19/10/2007 04:38:04 Md: 0.3
Epicentral Distance JS03: 13 km; JS06: 14.5 km

Figure 2. Three components (Z = horizontal, N = north–south, E = east–west) of two example recordings of two events. Even for small events ($M_d \leq 0.5$) waveform onsets were detectable. The grey boxes are indicating the error interval associated with the pick weight.

basement–sediment interface. Phase weighting was applied for both wave types based on estimated picking accuracy from 0 being the highest weight (pick uncertainty 0.02 s) to 3 being the lowest weight (pick uncertainty 0.4 s). For the *S*–*P* time used in SIMULPS for the calculation of the v_P/v_S ratio the weight of the *S* phase was applied. In total 655 local events were detected with magnitudes in the range of $-0.5 \leq M_d \leq 4.5$ while most of the events are in the magnitude range of $0 \leq M_d \leq 1$ (Braeuer *et al.* 2012). The presented waveform example in Fig. 2 is a good representation of the data set and shows the unusually good data quality even for small events. The magnitude of completeness (M_c: lowest magnitude at which 100 of the events in a space–time volume are detected, Rydelek & Sacks 1989) is about 0.5 (Braeuer *et al.* 2012).

Various authors described the importance of a careful selection of the initial model for LET studies (Kissling 1988; Eberhart-Phillips 1990; Kissling *et al.* 1994). As an initial model for the tomographic inversion we used the minimum—1-D model for *P* and *S* waves (Braeuer *et al.* 2012) with some small changes due to slightly different station configuration. The average of the 3-D velocities in each layer (weighted by the total ray length) is represented by the 1-D model, which is not biased by *a priori* input other than the choice of the layer depth and thickness (Kissling *et al.* 1994). Only events with 12 or more onset times were included, containing at least six *S*-wave observations, and a GAP (largest azimuth angle with no observation) <180°. This reduced the number to 530 well-constrained events consisting of 13 970 *P*- and 12 760 *S*-wave arrival time observations, that is, an average of 50 traveltime picks per event.

4 TOMOGRAPHY

We performed an iterative, simultaneous inversion of hypocentral parameters, v_P, and v_P/v_S ratios using the well-established

and widely used inversion code SIMULPS (Thurber 1983, 1993; Eberhart-Phillips 1986; Evans *et al.* 1994). A damped least-squares technique is used for the inverse solution of v_P and v_P/v_S, and subsequently hypocentres are relocated in the updated velocity model. For the forward problem the pseudo-bending approximate ray tracing (ART-PB) method is applied, developed by Um & Thurber (1987).

The chosen parametrization of the 3-D model should account for the distribution of earthquakes and stations and result in a homogeneous resolution throughout the volume. In Fig. 3(a) the ray
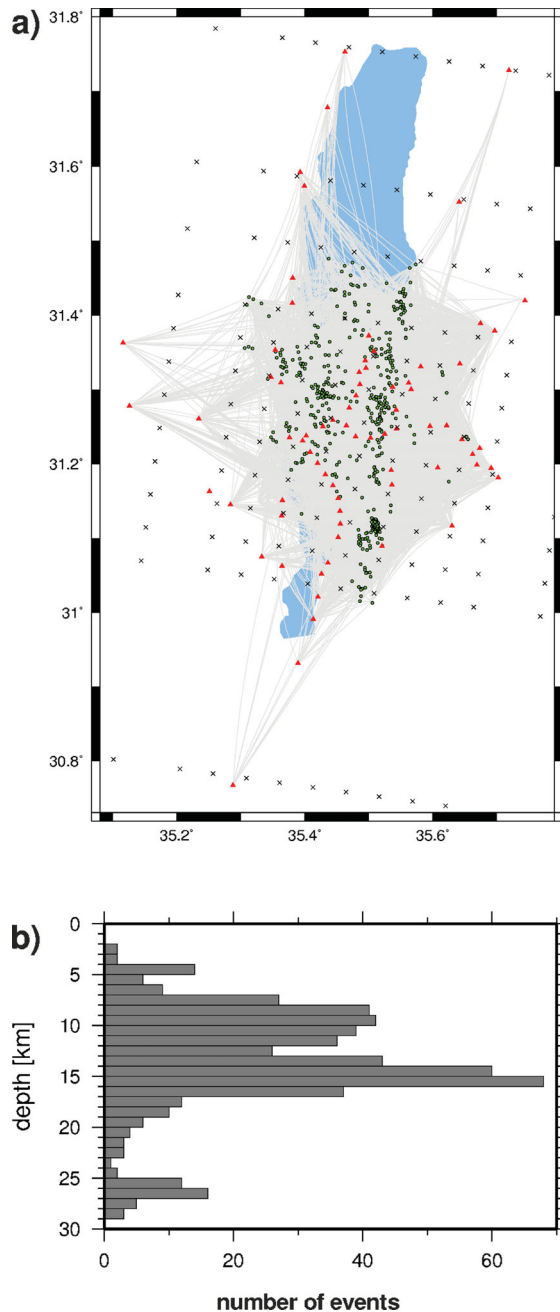
Table 1. Initial 1-D model for the tomography derived from the minimum—1-D—model for *P* and *S* waves (Braeuer *et al.* 2012) with some small changes due to different station configuration.

Depth (km)	v_P (km s^{-1})
0.0	3.90
5.0	4.55
10.0	5.36
15.0	5.36
20.0	5.36
30.0	5.36
100.0	8.00

coverage is shown together with the distribution of the events and the stations. The ray coverage was very dense around the EBF where most of the events occurred, station density was high and noise level was low. The WFs are covered by many rays despite the lower density of stations and events. Two model parametrizations were used to adapt the distances between the model nodes to the heterogeneous earthquake and station distribution: a coarse grid spacing of 10 × 10 km for the outer areas and a fine parametrization of 5 × 5 km for the area of dense station and earthquake distribution (Fig. 3). One node 30 km away to the north and one to the south, were added to account for some stations farther away. Vertical node spacing of 5 km was used until 20 km depth where the seismic activity decreases rapidly, followed by a node at 30 km depth (Table 1). For technical reasons one additional node is introduced at large distances (depth: 100 km; NS/EW: 750 km) following Evans *et al.* (1994). The number of observations and unknown variables for the inversion is shown in Table 2. To avoid problems with differences between the v_P and the v_S model (due to different ray paths, data quality, etc., Thurber 1993; Evans *et al.* 1994), SIMULPS uses *S–P* times to calculate v_P/v_S directly, starting with an initial average v_P/v_S value (1.74 from Wadati diagram analysis). Furthermore, the Poisson's ratio is directly related to the v_P/v_S ratio.

The 3-D inversion was performed following a gradual inversion scheme from, for example, Husen *et al.* (2000) where the complexity is increasing in each inversion: 1-D, 2-D and 3-D. The results of a previous inversion are used as initial model for the subsequent inversion. The gradual approach for a 3-D model is based on the assumption that in areas of low resolution, the true structure is better recovered by using a 2-D model as initial model than by using an initial 1-D model (Eberhart-Phillips *et al.* 1995). The goal of the 2-D inversion was furthermore to establish a regional model which reflects the dominant structural elements in the area. The small decrease in data variance together with the small increase in model complexity from the 2-D to the 3-D inversion in the gradual approach supports the assumption of a primarily 2-D structure of the volume under investigation (Table 3). A direct approach, without the intermediate step of a 2-D model, was also tested and all the discussed features in the velocity models were also found in this model.

The damping value is a critical parameter in LET. The damping determines the trade-off between model variance and the data variance. Low damping values will lead to high model perturbations with large reduction in data variance, whereas high damping values yield low model perturbations and small reduction in data variance. The appropriate damping value was selected empirically

Figure 3. (a) Ray paths of the 3-D SIMULPS inversion, indicated in grey. Final locations are plotted as green dots and the stations are marked with red triangles. The distance between the nodes of the inversion, indicated by crosses, range from 20 km at the edges of the model to 5 km in the centre. Map view where the model nodes are rotated 8° clockwise to align approximately with the main boundary faults trending NNE–SSW (see Fig. 1). (b) Histogram of events per depth kilometre.

Table 2. Number of observations and variables of the 3-D inversion.

	Knowns			Unknowns			
P-obs	S-obs	Total	model $x \times y \times z$ for v_P and v_P/v_S	Hypocentres	Origin times	Total	
			$16 \times 16 \times 9 \times 2$	3×530			
13970	12 760	26 730	4608	1590	530	6728	

Table 3. Data variance and model variance (only v_P) and rms of the three inversion steps: 2-D coarse inversion, 3-D coarse inversion and 3-D fine inversion.

	Spacing (km)	Data var. (s^2)	Per cent	Model var. (km^2 s^{-2})	rms	Per cent
Initial		0.204	100	0.013	0.540	100
2-D coarse (31 iterations)	5	0.036	18	0.101	0.240	44.4
3-D coarse (5 iterations)	5	0.033	16	0.111	0.234	43.3
3-D fine (5 iterations)	4	0.033	16	0.120	0.232	43.0
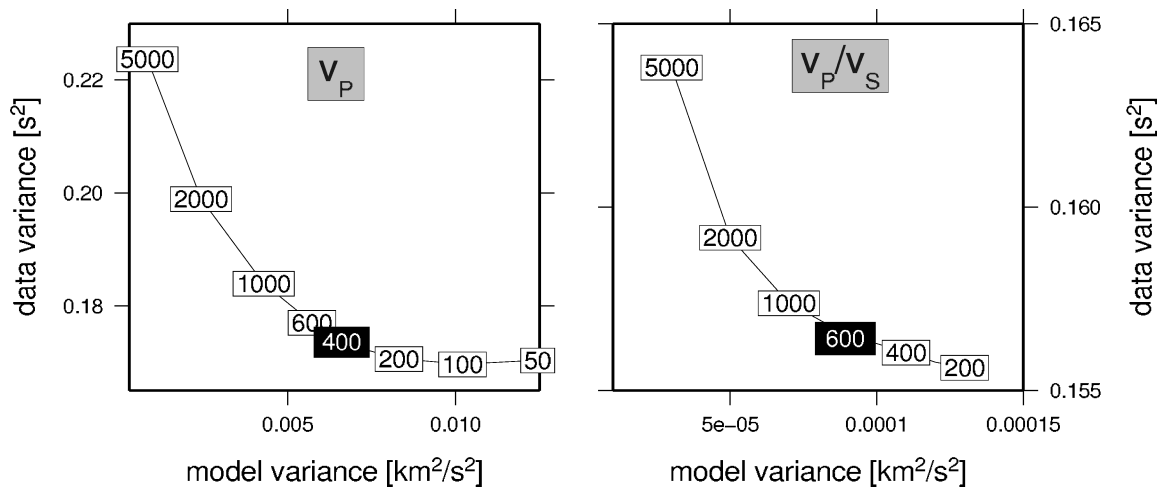
Figure 4. The model variance plotted versus data variance for different damping values for the direct 3-D inversion. The trade-off curves for v_P (left-hand side) and v_P/v_S (right-hand side) models are used to determine the preferred damping values, which are marked with black background colour.

from a series of one-step inversions with different damping values (Eberhart-Phillips 1986). The model variance values for the different inversions are plotted as a function of the data variance values to determine the trade-off curve (Fig. 4). The preferred damping values are chosen to achieve the best compromise between data misfit reduction and model variance. The v_P/v_S damping curve was calculated by using the previously determined P-damping factor (Fig. 4).

4.1 Resolution

An important part of a seismic tomography study is the assessment of the solution quality. Regions of good resolution need to be separated from poorly resolved ones (Kissling *et al.* 2001). In contrast to classical methods such as hit count or derivative weight sum (DWS), the full resolution matrix contains information about the interdependence between model parameters which influence the model resolution (Michelini & McEvilly 1991). The spread function derived from the resolution matrix is a measure of how strong

and peaked the resolution is at each node (Toomey & Foulger 1989; Eberhart-Phillips & Michael 1998, Fig. 5). By plotting the 70 per cent contour lines of the diagonal element for each resolution matrix (= smearing contours), the average contribution from neighbouring nodes and the dominant direction of any smearing is shown (Fig. 5, Eberhart-Phillips & Michael 1998). Following Toomey & Foulger (1989) and Kissling *et al.* (2001) resolution estimates based on spread values still depend on the damping values and the model parametrization. The threshold which defines the range of acceptable spread values is therefore not universally applicable. The choice of the threshold is thus based on the ray coverage, the relative size of the spread value, the smearing contours and on the results of synthetic tests. The threshold was determined to 2.0 for v_P and 2.2 for v_P/v_S.

In Fig. 5 the spread values and the smearing contours for the final v_P and v_P/v_S models in 2-D and 3-D are shown. The smearing contours are shown only for those nodes that have smearing, such that the smearing contour extends beyond an adjacent node and if the spread value is below the threshold. While in the 2-D model only minor smearing at the borders appears, in the 3-D v_P/v_S model even
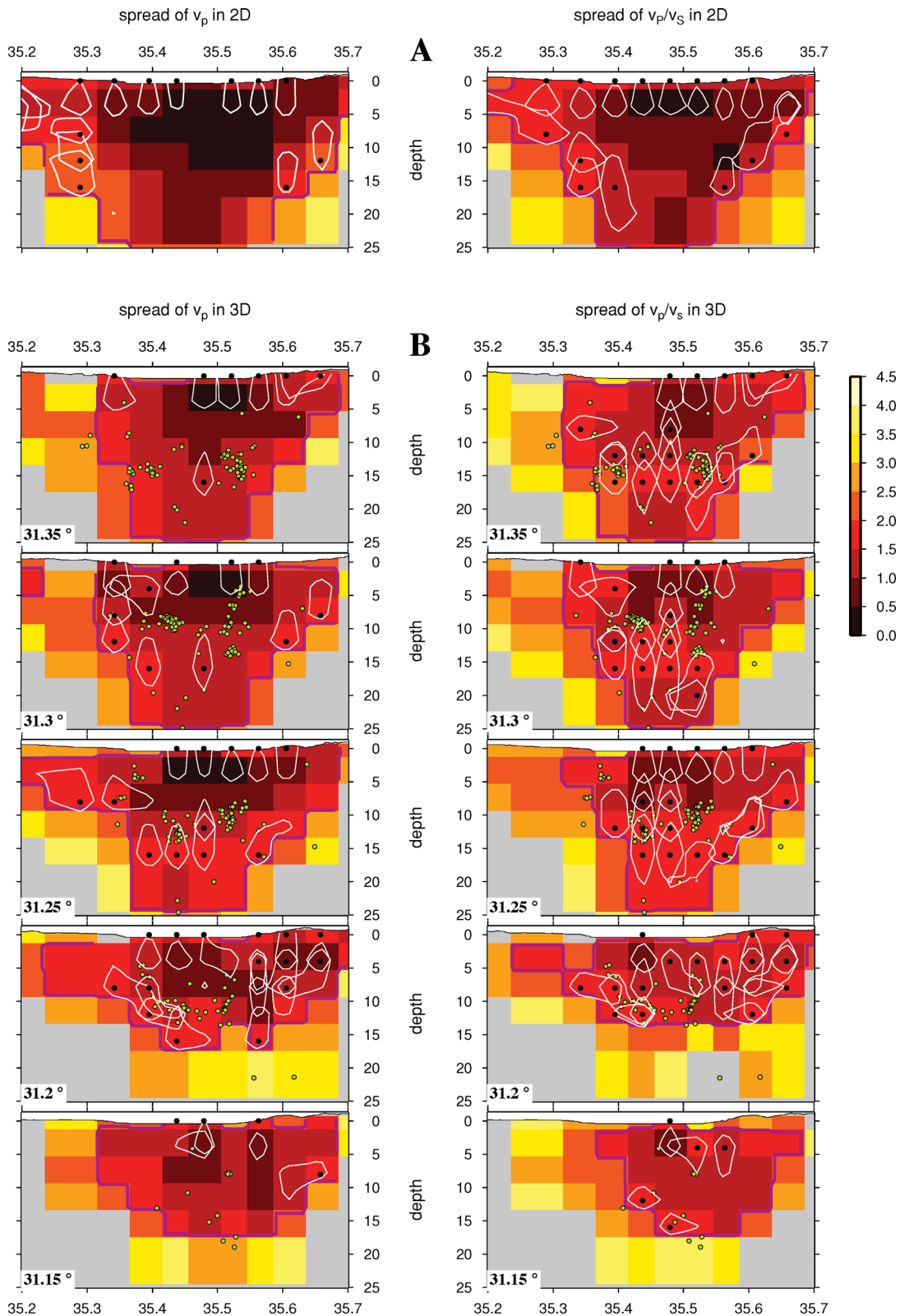
Figure 5. Longitude–depth sections of spread values of the model resolution matrix for the final 2-D model (A) and the final 3-D model (B) of the real data. (left-hand side) v_P nodes; (right-hand side) v_P/v_S nodes. Spread values are shown with different colours, superimposed are the 70 per cent contour line (white) of the resolution kernel, indicating the smearing. Green dots indicate events within ±2.5 km around the section. The violet contour lines border regions with acceptable resolution, determined together with the synthetic tests [threshold 2 (v_P) and 2.2 (v_P/v_S)].

nodes in the centre are influenced by adjacent nodes. Furthermore, for all models significant smearing occurs from the uppermost node downwards, which should be considered in the discussion of the velocities in the uppermost layer.

A widespread method to assess the resolving capacity of the given model configuration involves synthetic checkerboard tests. Checkerboard models are built up of laterally and vertically alternating positive and negative velocity perturbations of a background model. Whether the regular structure of the checkerboard model is recovered or not helps to distinguish regions of different resolution capacity. However, checkerboard tests show only the ability of the data to resolve the fine-scale structure and therefore do not imply that large-scale structures are resolved as well. Restoring resolution tests use the obtained inversion results as an input model to calculate synthetic traveltimes (e.g. Zhao *et al.* 1992) to estimate the capacity of the data set to resolve the geometry and amplitude of the velocity model. Haslinger *et al.* (1999) and Husen *et al.* (2000) enhanced this concept by designing a synthetic model, called the 'characteristic model', that is based on the inversion results obtained with the real data. This characteristic model retains the sizes and amplitudes of the velocity anomalies revealed by the inversion but has different geometry and a different sign of the velocity variation (Husen *et al.* 2000). The 2-D velocity structures revealed by the real data are rather simple: The *P*-wave model shows a strong negative *P*-wave velocity anomaly in the area of the basin down to a depth of 18 km. The distribution of the v_P/v_S ratio shows high values within the basin with an inclined lower boundary and lower values at the shoulders. Therefore, we constructed 2-D synthetic models with different depth and shape of the lower boundary of the velocity anomalies, shown in Fig. 6. Synthetic traveltimes were computed by the ray tracer implemented in SIMULPS (ART-PB method; Um & Thurber 1987), using the same source–receiver distribution and model parametrization as for the real data. Gaussian-distributed noise was added with a standard deviation of 0.05 for highest quality readings (weight 0) increasing to 0.5 for lowest quality readings (weight 3). In the last step the resulting traveltimes were inverted using the original station and event distribution.

In Fig. 6 the synthetic input models for the *P*-wave velocity model (first column) and the model of v_P/v_S ratios (third column) are shown along with the recovered models from the inversion (second and fourth column, respectively). Symmetric and asymmetric velocity anomalies with depths of 8, 12 and 16 km are tested for the *P*-wave velocity model and the model of v_P/v_S ratios. The intensity of the velocity anomalies is the same as in the real model. The recovery of the *P*-wave velocity models is nearly perfect. The recovered models of v_P/v_S ratios confirm the smearing for the uppermost layer already observed by the smearing contours in Fig. 5. Furthermore, the anomalies down to 16 km depth are not perfectly recovered. However, all different recovery models are clearly distinguishable. Hence the station and earthquake distribution of the investigation area is able to model the principal structure of the basin.

The differences between the 2-D model and the 3-D model are small compared to the difference between the 1-D initial model and the 2-D model (see Table 3). Thus, for the 3-D model checkerboard tests, with rather small velocity, variations are more reasonable when using the gradual approach. The checkerboard model is generated by superimposing the initial velocity model with velocity perturbations of ±5 per cent of the absolute velocity value (Fig. 7). In the same way as for the restoring resolution tests, the calculated traveltimes are disturbed with noise and again inverted using the original experimental setup. The results for the checkerboard tests

are shown in longitude–depth sections in Fig. 7 for the *P*-wave velocity model and the model of v_P/v_S ratios, respectively. Between 35.35° and 35.55°E longitude and until a depth of 12 km the perturbations are well restored, affirming the good ray coverage within the basin and near to its boundaries. Furthermore, in the north until 31.25°N latitude the well-restored part reaches a depth of 16 km for the v_P/v_S model and 20 km for the *P*-wave model due to deeper earthquakes in the north. The smearing of the nodes at 0 km depth into the nodes at 4 km depth, already displayed by the smearing contours (Fig. 5), is also observed in all sections.

5 RESULTS

5.1 2-D model

The main feature of the tomographic models is expected to be 2-D, determined by the sedimentary basin. The v_P model is represented by absolute values, by velocity–depth functions, as well as by deviations from the 1-D initial model (Figs 8a–c). The tomography revealed *P*-wave velocities at the surface of about 3.5 km s^{-1} in the basin and about 4 km s^{-1} at the shoulders west of 35.35°E and east of 35.55°E. The difference between former investigations (e.g. tomography data from active seismics; Paschke *et al.* 2012) and the results of this study is due to the large smearing of the shallowest model node of the inversion to the model node at 4 km depth (see Fig. 5). Therefore the steep velocity gradient commensurate with the expected compaction of the basin fill (ten Brink & Flores 2012) is not observed. At the shoulders the velocity is increasing with a constant gradient to about 5.5–6 km s^{-1} at about 8 km depth (Fig. 8). The basin between 35.43°E and 35.52°E exhibits a marginal velocity gradient, resulting in velocities of only about 4–4.5 km s^{-1} at 8 km depth. At 16 km depth, velocities of less than 5 km s^{-1} are observed, indicating a strong velocity reduction compared to the regions east and west of the basin.

The difference between the basin and the shoulders is revealed even more clearly when the v_P model is displayed as deviations from the background model (Fig. 8c). Between 35.35°E and 35.55°E the *P* velocities are up to 25 per cent slower than in the background model. Similarly large differences to the background model are found in other sedimentary basins, for example, in eastern Turkey (Kaypak 2008) and in southern California (Lin *et al.* 2007). The lower boundary of the relatively low velocities is reached at 18 km depth. At 18 km depth a velocity of 5.3 km s^{-1} is observed, which is the value used to define the lower boundary of the basin sediments by ten Brink & Flores (2012). The eastern boundary of this low-velocity zone, where also a large part of the seismicity is concentrated, is vertical from the surface down to the lower boundary (Fig. 8c). The western boundary is inclined to the east in the uppermost 7 km.

The model of the v_P/v_S ratios in Fig. 8(d) is characterized by distinct areas of high (above the average of 1.74) and low (below the average of 1.74) ratios. West of 35.35°E and east of 35.55°E low values are observed from surface to depth. The basin is characterized by high values from the surface to about 7 km depth. At the western boundary below this depth the ratios change to average values of 1.74 and below. The high values at the eastern boundary reach about 12 km depth.

The shallow structure is thus similar in the v_P model and in the model of the v_P/v_S ratios (Fig. 8d) with a vertical eastern boundary and an inclined western boundary. However, the lower boundary is about 18 km for the v_P model but only 7–12 km for the model
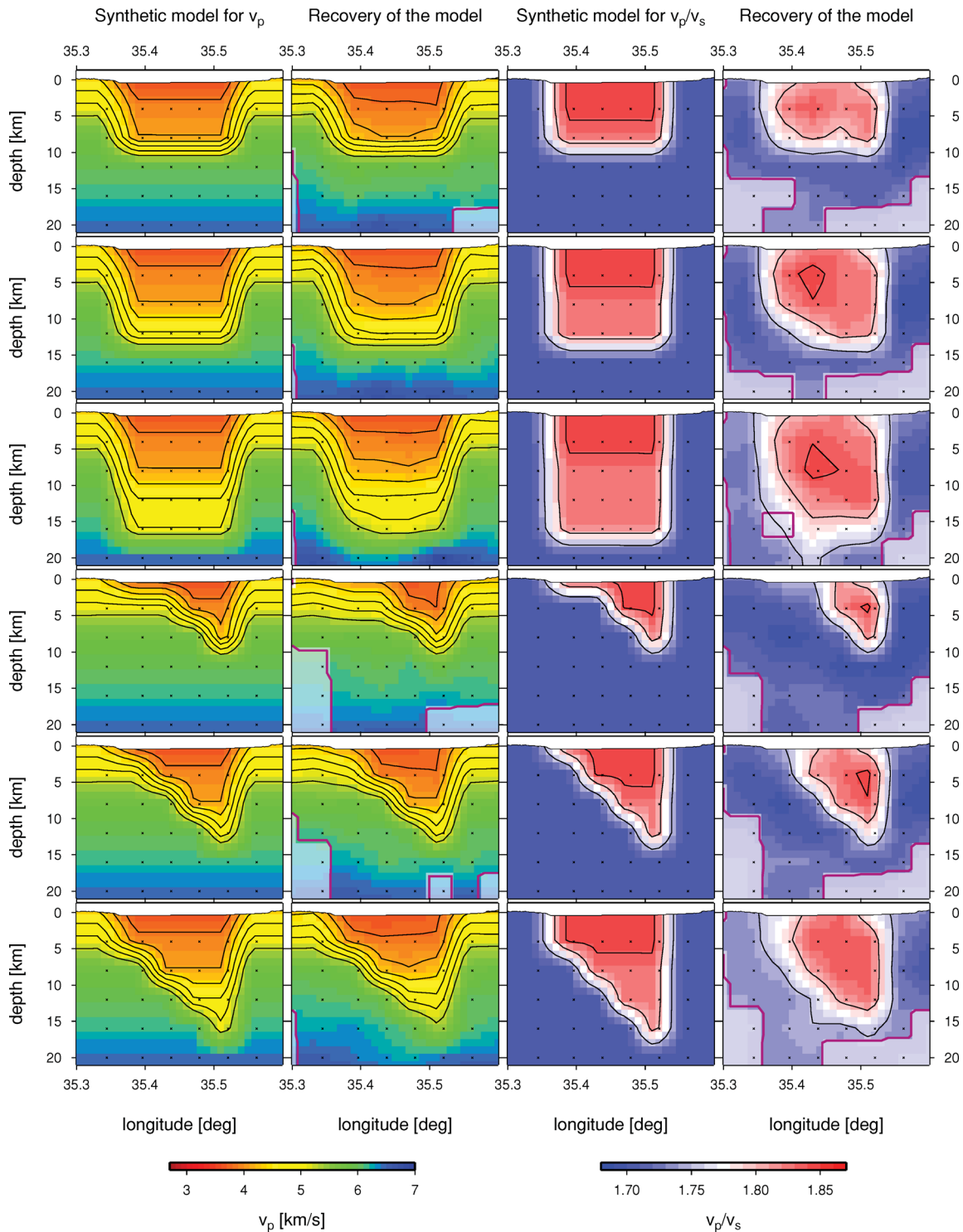
Figure 6. Assessment of the resolution for the expected sedimentary basin characterized by low *P*-wave velocities (left-hand side) and high v_P/v_S ratios (right-hand side), respectively. Longitude–depth sections of synthetic model recovery tests. Contour lines of the *P*-wave velocities and the v_P/v_S ratios are indicated as thin black lines. Regions with lower resolution are faded. The violet contour encloses regions of good resolution defined by the spread value in combination with the synthetic tests. Model nodes are indicated by crosses.

of the v_P/v_S ratios (Fig. 8). The locations of the boundaries are not a result of the gridpoint distribution. In the Appendix it is shown that the lower boundaries of the areas of low v_P and high v_P/v_S ratios remain at the same place when the gridpoint location is changed.

5.2 3-D model

The principal pattern of the *P*-wave velocity distribution in 3-D is similar to the 2-D v_P model. The area of the basin displays lower absolute *P*-wave velocity values then the shoulders (Figs 9a and 10
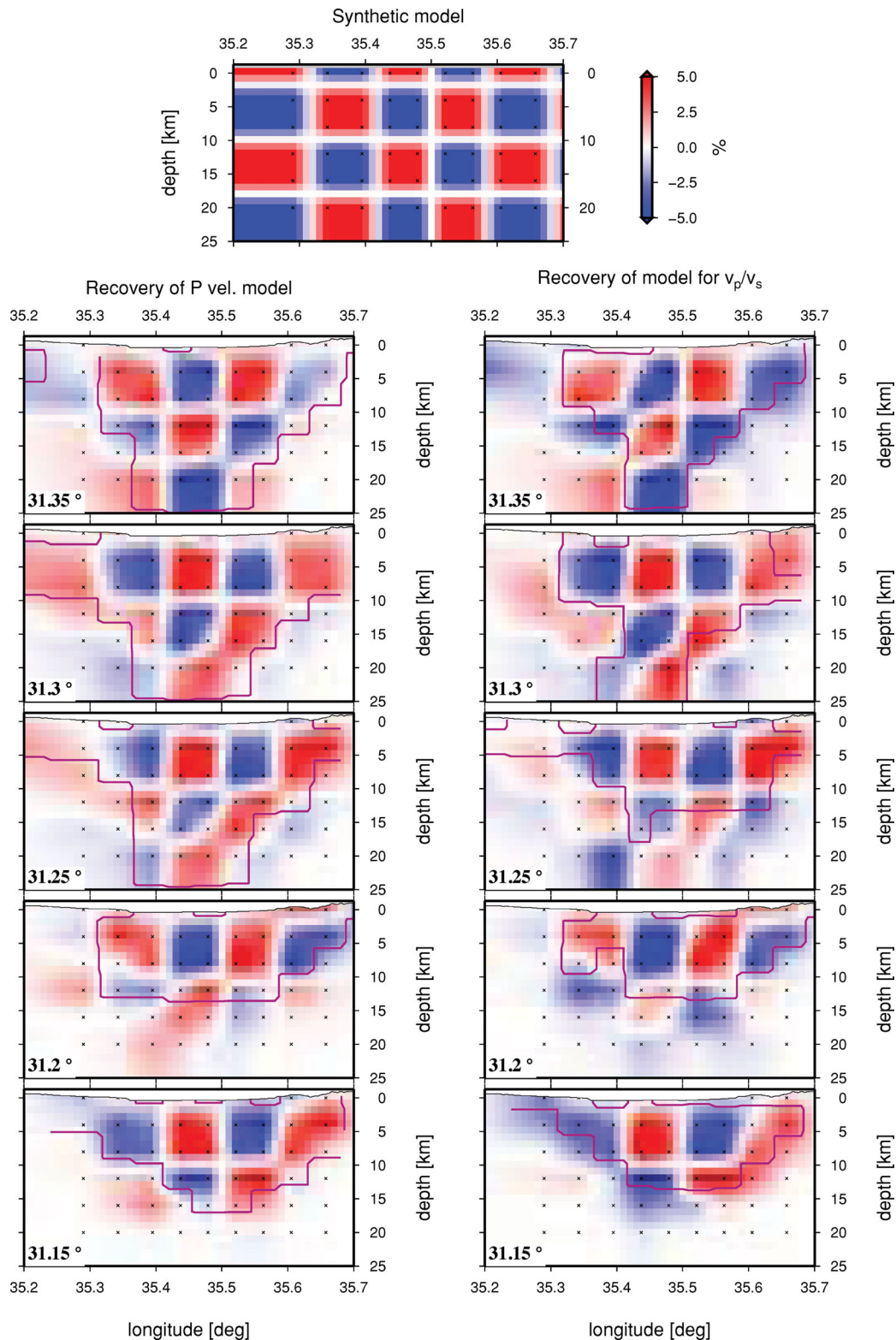
Figure 7. Longitude–depth sections of the original checkerboard model (top most) and the reconstruction of the synthetic v_P model (left-hand column) and the model of v_P/v_S ratios (right-hand column) at different latitudes. The violet contour encloses regions of good resolution defined together with the spread value. Crosses indicate the model nodes.

left-hand side) and lower *P*-wave velocities than the background model (5–25 per cent lower, Figs 9b and 10 right-hand side). The eastern boundary of the low-velocity body is located in the area of the EBF from the surface down to at least 17 km depth. How-

ever, due to the rapid decrease of the number of earthquakes below 17 km depth (Braeuer *et al.* 2012, Fig. 3b), the resolution of the deeper part is limited (see Figs 5 and 7). The western boundary of the low-velocity body is located in the area of the WF near the surface
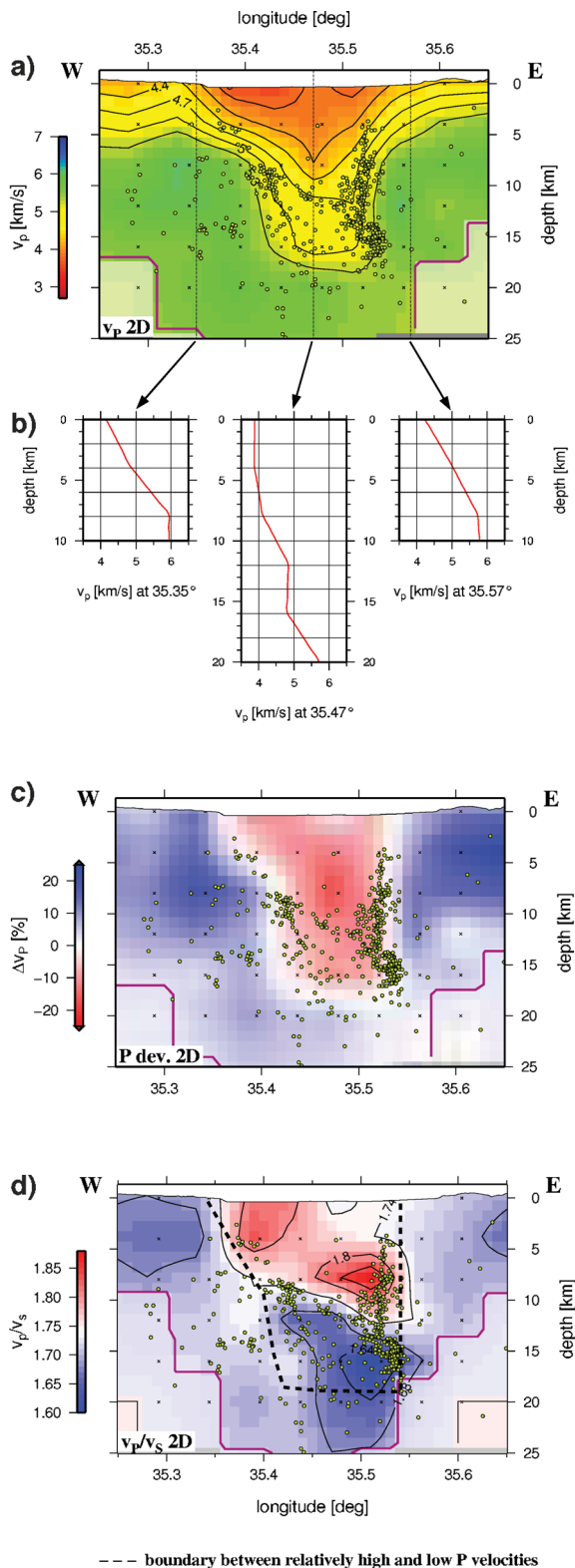
Figure 8. Results of the 2-D tomographic inversion: (a) Absolute *P*-wave velocity model with contour lines. (b) Velocity–depth functions at three different longitudes. (c) Deviations of v_P from the background model. (d) Model of the v_P/v_S ratios with contour lines, dashed line is indicating the border of the low v_P body. Note the larger depth extent of the v_P anomaly. Regions with lower resolution are faded. The green dots are indicating the earthquakes. The violet contour encloses regions of good resolution. Model nodes are indicated by crosses.

and more eastwards with increasing depth (down to 11 km depth), reflecting the inclined western boundary (Figs 9b and 10 right-hand side). The inclined western boundary and the steep to vertical EBF is also reflected by the contour line of 5.3 km s^{-1} (Fig. 10 left-hand side). In the central three sections (latitude: 31.2–31.3°N) the lower boundary of the low *P*-wave velocity body is reached between 17 and 18 km depth (Figs 9b and 10 right-hand side), where also the 5.3 km s^{-1} contour is reaching its greatest depth (Figs 9a and 10 left-hand side). The same boundaries are found at depth of 16 km in the north (31.35°N) and at 20 km in the south (31.15°N). Several small high-velocity anomalies appears in the absolute *P*-wave velocity models (Figs 9a and 10 left-hand side), partly resulting in low velocity zones below them. As they are limited to only one or two grid nodes and appear mostly at the edge of the model, these are most likely artefacts of the inversion, indicating the limits of our data set for a full 3-D inversion. A large part of the seismicity can be assigned to the EBF. However, many events occur between 10 and 15 km depth within the low *P*-wave velocity body (Figs 9 and 10).

Strong contrasts are observable in the model of v_P/v_S ratios (Fig. 11). High ratios (>1.8) are characterizing the basin down to a depth of at least 7 km. However, around 31.3°N/35.5°E average values of 1.74 and lower appear between 2 and 5 km depth. The highest v_P/v_S ratios (up to 2) are found between 2 and 5 km depth south of 31.2°N and north of 31.35°N (Fig. 11). Below the Lisan Peninsula around 31.3°N/35.5°E in 8 km depth values slightly above the average value of 1.74 are revealed (Fig. 11). The seismicity can be assigned to the boundary faults and the change between high and low v_P/v_S ratios.

In Fig. 12 a north–south profile in the eastern part of the basin (for exact location see Fig. 1) clearly displays a contrast in the v_P/v_S ratio. It is between 10 and 14 km deep with minimum depth at kilometre −15 (area of the Boqeq Fault) and maximum depth at kilometre 5 (below Lisan Peninsula). The area below the Lisan Peninsula, characterized by ratios of 1.7 and below, extends from kilometre 5 to −9 down to depth of 5–6 km. The different areas of upper crustal seismic activity north and south of the Boqeq Fault, already found by Braeuer *et al.* (2012), can be assigned to areas of different seismic properties. In the south (south of km −15) the solely active EBF (Braeuer *et al.* 2012) shows activity in the area of low v_P/v_S and low v_P. However, in the north (north of km −15) the seismic activity is found in areas of medium to high v_P/v_S ratios and low v_P.

6 DISCUSSION

Certain features of the v_P model and the model of v_P/v_S ratios are similar, though some important differences between them exist. Both 2-D models show a similar structure for the uppermost 8 km (Fig. 8). The sedimentary basin is clearly imaged through low *P* velocities and high v_P/v_S ratios. The eastern boundary of the sedimentary body is vertical while the western boundary is inclined to the east (Figs 8 and 10). Thus, an asymmetric structure of the sedimentary basin is revealed through both models. The difference between both boundaries in the southern DSB is also obvious from observations of the seismicity from our data set (Figs 8 and 9; Braeuer *et al.* 2012) and other investigations. The EBF is traceable vertically from 4 km depth down to 17 km depth exactly below its surface trace (Figs 8 and 9; Braeuer *et al.* 2012). The large earthquakes as well as the microseismic activity in the southern DSB is concentrated at the EBF (van Eck & Hofstetter 1989; Salamon *et al.* 2003; Shamir 2006; Hofstetter *et al.* 2008; Abou
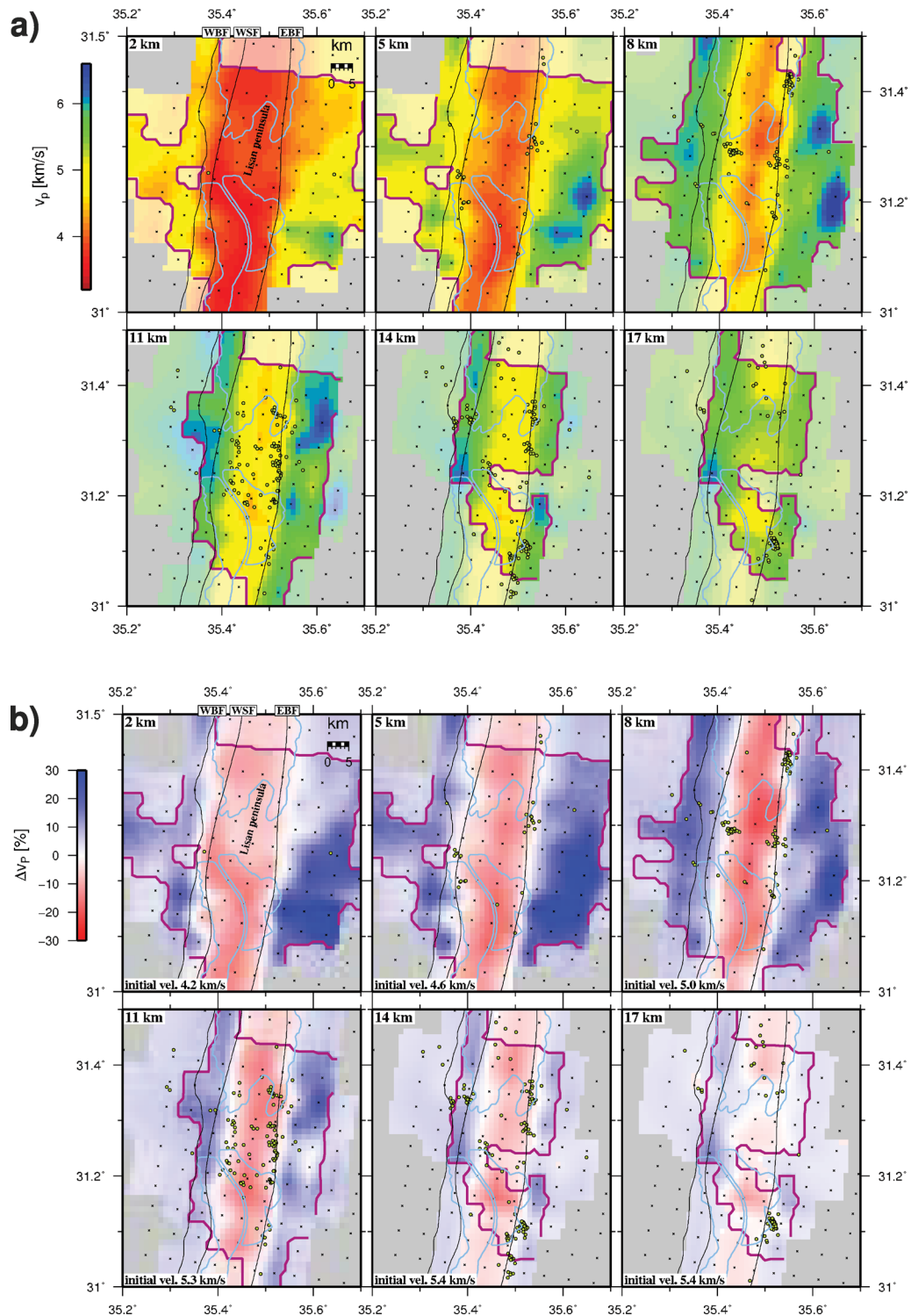
Figure 9. Depth maps of the 3-D v_P velocity model, displayed as absolute values (a) and as deviations from the 1-D starting model (b). Depths are indicated in the upper left corner. Earthquakes within 3 km of the layer are plotted as green dots while the model nodes are indicated by black crosses. Regions with lower resolution are faded, whereas unresolved regions are coloured in grey. The violet contour encloses regions of good resolution defined by the spread value in combination with the synthetic tests. Fine black lines are indicating the boundary faults, light blue lines the coastline.

Elenean *et al.* 2009). The only large event associated with the western boundary occurred on 1927 June 11 (*M* = 6.2), while the poor recording situation at that time resulted in ambiguities of the location (Avni *et al.* 2002, and references therein). The western boundary is built up by several faults, the WSF, the continuation of the Jericho Fault and various normal faults, where the WBF is the most impor-

tant one (e.g. Garfunkel 1997). No seismicity concentration clearly assignable to one specific fault is observable. The seismicity associated with the western boundary initiates westwards of both faults and continues until eastwards of them (Figs 8–10, Braeuer *et al.* 2012). Sagy *et al.* (2003) found four sets of oblique-normal faults at the western boundary and their 3-D fault modelling revealed large
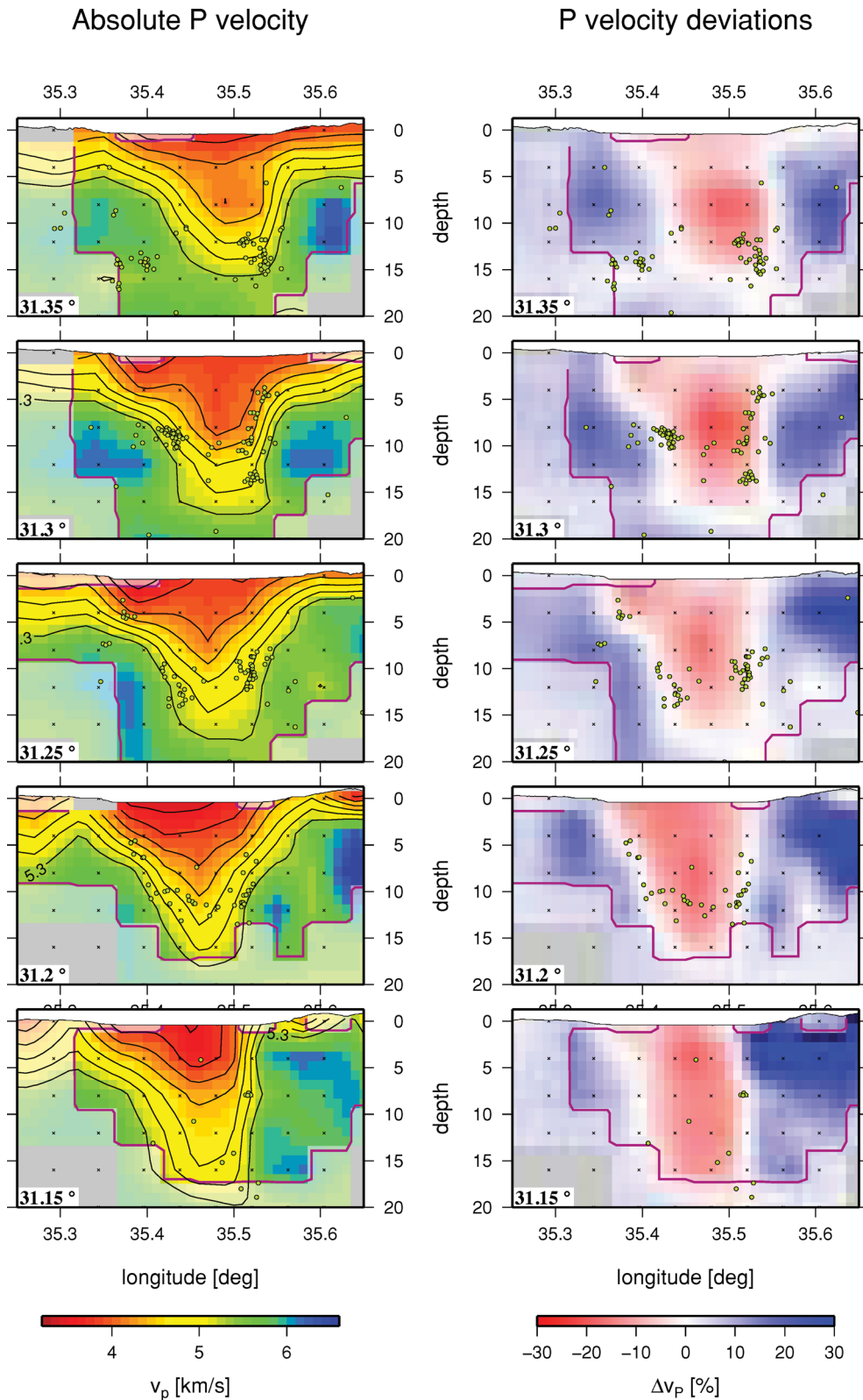
Absolute P velocity

P velocity deviations

Figure 10. West–east depth sections through the 3-D v_P model, displayed as absolute values (left column, with contour lines) and as deviations from the 1-D starting model (right column). Latitudes are indicated in the lower left corner. Earthquakes within 5 km of the section are plotted as green dots while the model nodes are indicated by black crosses. Regions with lower resolution are faded, whereas unresolved regions are coloured in grey. The violet contour encloses regions of good resolution defined by the spread value in combination with the synthetic tests.
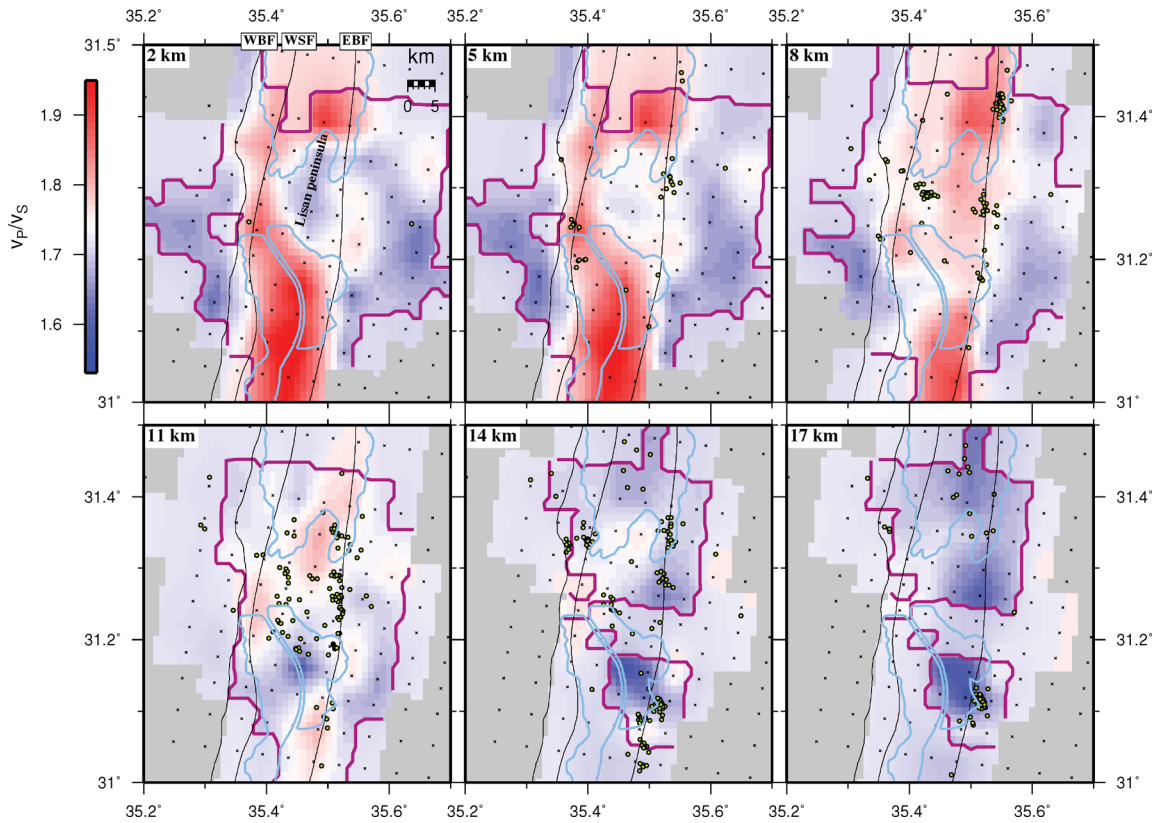
Figure 11. Depth maps of the 3-D model of v_P/v_S ratios. Depths are indicated in the upper left corner. Earthquakes within 3 km of the section are plotted as green dots while the model nodes are indicated by black crosses. Regions with lower resolution are faded, whereas unresolved regions are coloured in grey. The violet contour encloses regions of good resolution defined by the spread value in combination with the synthetic tests. Fine black lines indicate the boundary faults, light blue lines the coastline.
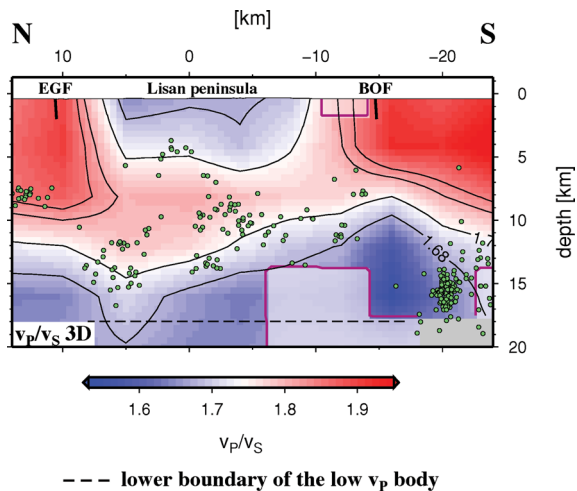

Figure 12. North–south depth section through the 3-D model of v_P/v_S ratios with contour lines in the eastern part of the basin. It is rotated 8° clockwise to align approximately with the main boundary faults trending NNE–SSW (see Fig. 1). The Boqeq Fault (BOF) and the Ein Gedi Fault (EGF) are indicated. Earthquakes within 8 km of the section are plotted as green dots. Regions with lower resolution are faded, whereas unresolved regions are coloured in grey. The violet contour encloses regions of good resolution defined by the spread value in combination with the synthetic tests.

horizontal E–W extension. Furthermore, magnetic measurements from Frieslander & Ben-Avraham (1989) in the northern part of the basin confirm the differences between the eastern and the western boundary. These authors found magnetic anomalies crossing the WF uninterrupted, indicating normal faulting along the western side of the basin. Meanwhile, across the eastern border fault magnetic contours are displaced, suggesting predominant strike-slip motion resulting in major lithological changes across the EBF (Frieslander & Ben-Avraham 1989). Physical analogue modelling of Rahe *et al.* (1998) showed that asymmetric basin geometry appears when one side of a pull apart basin is fixed in place (here the western boundary) while most of the strike-slip movement occurs at the other side (here the EBF). Similar asymmetries have been observed in many other sedimentary basins in strike-slip regimes (e.g. Shedlock *et al.* 1990; Lodolo *et al.* 2003; Uzel & Sözbilir 2008) and also in other basins along the DST (Ben-Avraham 1992). Analogue tectonic modelling experiments (Smit *et al.* 2010) of the DST suggest that the change in plate kinematics *ca.* 5 Myr (already suggested by Garfunkel 1981, due to a change of the Eulerian pole of relative plate motion) caused a transtensional deformation for the southern part of the DST. This would cause extensional structures as, for example, the normal faults at the western boundary.

The Lisan salt diapir below the Lisan Peninsula is imaged through v_P/v_S ratios below the average of 1.74 (Fig. 11). However, the v_P model shows no features in this area (Fig. 9). In magnetotelluric measurements the salt body is characterized by very high resistivity, indicating the absence of fluids necessary for electric conductivity (Meqbel *et al.* 2012). The diapir extends from the eastern boundary

about 12 km to the west. The maximal NS elongation of the diapir is estimated to be about 17 km while the lower limit of the salt body is reached at depths between 5 and 6 km (Fig. 12). These values are in good agreement with estimations based on gravity measurements from (Choi *et al.* 2011) who suggested a size of 10×20 km and a depth of about 6 km while Al-Zoubi & ten Brink (2001) estimated from seismic reflection data a size of 10×13 km and a depth of 7 km. The Pleistocene sediments farther west of the diapir show very low resistivity (Meqbel *et al.* 2012) and high v_P/v_S ratios (Fig. 11), indicating significant fluid content. The sediments deposited during the basin subsidence (younger than ~ 17 Myr) are of fluvial, lacustrine and marine origin (Garfunkel 1997; Garfunkel & Ben-Avraham 2001). Except for salt, these sediments are thus expected to have a significant fluid content. Thus, the region of high v_P/v_S ratios is most likely indicating the basin fill sediments (Figs 8d, 11 and 12). Its average lower boundary at the western edge of the basin from our tomography study at about 7 km depth (Fig. 8d) was also determined by a borehole study of (Gardosh *et al.* 1997) located south of the Sedom diapir (below Mt Sedom, Fig. 1). Due to the limited resolution in the western edge of the basin, changes in NS direction cannot be verified (Figs 5 and 7). While the average lower boundary of the basin fill sediments in the eastern edge of the basin is at about 12 km depth (Fig. 8d), significant changes occur on a N–S profile (Fig. 12). Below the Lisan Peninsula the lower boundary occurs at about 14 km depth, the same depth where Ginzburg & Ben-Avraham (1997) found their lowest refractor in a N–S refraction seismic profile. The depth of the lower boundary decreases towards the south and reaches about 10 km depth at the Boqeq Fault. This inclination is in good agreement with the decrease of the negative gravity anomaly at the same location in ten Brink & Flores (2012).

A significant difference between the v_P model and the model of v_P/v_S ratios appears in the lower part of the sedimentary basin (depth >8 km, Fig. 8d). The low v_P body forms a nearly horizontal lower boundary of about 10 km width and extends to a depth of about 18 km (Figs 8 and 10). Slightly reduced P velocities down to 18 km depth were also observed by ten Brink *et al.* (2006) from a 250-km-long EW seismic refraction experiment crossing the DSB at about $30.9°$N. Another seismic refraction experiment presented by Mechie *et al.* (2009) crossed the DSB at the Lisan Peninsula. While their final model shows only slightly reduced P-wave velocities between 11 and 18 km depth below the basin, the authors state that models with P-wave velocities lower than 5.6 km s^{-1} fit the data equally well. These values are just assumed to be unrealistic (Mechie *et al.* 2009). Furthermore, a significant decrease of seismic activity appears at 18 km depth—in our data set (Figs 3b and 8; Braeuer *et al.* 2012) as well as in a long-term observation of Hofstetter *et al.* (2012).

The pre-basin sediments on the shoulders of the basin are characterized by P-wave velocities of about 5 km s^{-1} and relatively low v_P/v_S ratio (<1.7, Fig. 8, Paschke *et al.* 2012). The same characteristics are found for a 4- to 8-km-thick layer below the basin fill sediments (Figs 8 and 12). However the pre-basin sediments outside the DSB are only ~ 3 km thick (e.g. Garfunkel 1997; Mechie *et al.* 2009) and expected to be even thinner within the basin due to the stretching of the basin. Husen *et al.* (2004) found in a volcanic field low P-wave velocities and low v_P/v_S ratios, interpreted as porous, fluid-filled rocks. Stern *et al.* (2001) found beneath the Alpine transform Fault in New Zealand reduced P-wave velocities caused by high fluid pressure. Therefore, we agree with the interpretation of ten Brink & Flores (2012) who explained the reduced P-wave velocities down to 18 km depth below the basin with the

influx of fluids from the surrounding crust and/or the upper mantle. The interaction of the fluids with the lower crust profoundly weakened the yield strength, causing the rapid subsidence within the past 1 Myr (ten Brink & Flores 2012, and references therein). The microseismic activity in the lower crust (Aldersons *et al.* 2003; Hofstetter *et al.* 2012; Braeuer *et al.* 2012, Fig. 3b) is then explained by rapidly rising fluids, creating locally hydro-fracturing even within the ductile crust (ten Brink & Flores 2012).

7 CONCLUSIONS

In this study local earthquake data from a dense temporary seismological network in the southern Dead Sea area have been analysed within the project DESIRE. Local earthquakes are used for the first precise image of the distribution of the P-wave velocity and the v_P/v_S ratios, using tomographic inversion techniques.

The basin fill sediments are characterized by low P-wave velocities and high v_P/v_S ratios, reaching average depths of about 7 km in the western edge of the basin which is verified by a borehole study (Gardosh *et al.* 1997). In the eastern edge of the basin the lower boundary of the basin fill sediments varies between 10 and 14 km. This asymmetric structure of the basin fill is caused by the normal faulting at the western boundary, confirming the recent transtensional regime in the basin (Garfunkel 1981; Smit *et al.* 2010).

The Lisan salt diapir shows low v_P/v_S ratios, reflecting its low fluid content. The extensions were determined to 12 km in E–W and 17 km in N–S direction, confirming former investigations (Al-Zoubi *et al.* 2002; Choi *et al.* 2011), while its depth was determined to 5–6 km.

The thickness of the pre-basin sediments below the basin fill cannot be derived from the tomography data—it is estimated to less then 3 km from former investigations.

Below the basin, down to 18 km depth very low P-wave velocities and low v_P/v_S ratios is caused by the influx of fluids from the surrounding crust and/or the upper mantle (ten Brink & Flores 2012).

REFERENCES

Abou Elenean, K.M., Aldamegh, K.S., Zharan, H.M. & Hussein, H.M., 2009. Regional waveform inversion of 2004 February 11 and 2007 February 09 Dead Sea earthquakes, *Geophys. J. Int.,* **176,** 185–199, doi:10.1111/j.1365-246X.2008.03971.x.

Al Zoubi, A. & ten Brink, U.S., 2001. Salt diapirs in the Dead Sea basin and their relationship to Quaternary extensional tectonics, *Mar. Pet. Geol.,* **18,** 779–797.

Al Zoubi, A., Shulman, H. & Ben-Avraham, Z., 2002. Seismic reflection profiles across the southern Dead Sea basin, *Tectonophysics,* **346,** 61–69.

Aldersons, F., Ben-Avraham, Z., Hofstetter, A., Kissling, E. & Al Yazjeen, T., 2003. Lower-crustal strength under the Dead Sea basin from local earthquake data and rheological modeling, *Earth planet. Sci. Lett.,* **214,** 129–142.

Avni, R., Bowman, D., Shapira, A. & Nur, A., 2002. Erroneous interpretation of historical documents related to the epicenter of the 1927 Jericho earthquake in the Holy Land, *J. Seismol.,* **6,** 469–476.

Ben-Avraham, Z., 1992. Development of asymmetric basins along continental transform faults, *Tectonophysics,* **215,** 209–220.

Ben-Avraham, Z. & Schubert, G., 2006. Deep 'drop down' basin in the southern Dead Sea, *Earth planet. Sci. Lett.,* **251,** 254–263.

Ben-Avraham, Z. & Ten Brink, U., 1989. Transverse faults and segmentation of basins within the Dead Sea Rift, *J. Afr. Earth Sci.,* **8,** 603–616.

Ben-Avraham, Z. & Zoback, M.D., 1992. Transform-normal extension and asymmetric basins: an alternative to pull-apart models, *Geology,* **20,** 423–426.

Braeuer, B., Asch, G., Hofstetter, R., Ch. Haberland, Jaser D., El-Kelani, R. & Weber, M., 2012. Microseismicity distribution in the southern Dead Sea basin and its implications on the structure of the basin, *Geophys. J. Int.,* **188,** 873–878, doi:10.1111/j.1365-246X.2011.05318.x.

Choi, S., Götze, H.-J., Meyer, U. & DESIRE Group, 2011. 3-D density modelling of underground structures and spatial distribution of salt diapirism in the Dead Sea Basin, *Geophys. J. Int.,* **184,** 1131–1146, doi:10.1111/j.1365-246X.2011.04939.x.

van Eck, T. & Hofstetter, A., 1989. Microearthquake activity in the Dead Sea region, *Geophys. J. Int.,* **99,** 605–620.

Eberhart-Phillips, D., 1986. Three-dimensional velocity structure in northern California Coast Ranges from inversion of local earthquake arrival times, *Bull. seism. Soc. Am.,* **76,** 1025–1052.

Eberhart-Phillips, D., 1990. Three-dimensional P and S velocity structure in the Coalinga region, California, *J. geophys. Res.,* **95**(B10), 15 343–15 363.

Eberhart-Phillips, D. & Bannister, S., 2010. 3-D imaging of Marlborough, New Zealand, subducted plate and strike-slip fault systems, *Geophys. J. Int.,* **182,** 73–96.

Eberhart-Phillips, D. & Michael, A.J., 1998. Seismotectonics of the Loma Prieta, California, region determined from three-dimensional V_P, V_P/V_S, and seismicity, *J. geophys. Res.,* **103**(B9), 21 099–21 120.

Eberhart-Phillips, D., Stanley, W.D., Rodriguez, B.D. & Lutter, W.J., 1995. Surface seismic and electrical methods to detect fluids related to faulting, *J. geophys. Res.,* **100**(B7), 12 919–12 936.

Evans, J.R., Eberhart-Phillips, D. & Thurber, C.H., 1994. User's manual for SIMULPS12 for imaging V_P and V_P/V_S: a derivative of the 'Thurber' tomographic inversion SIMUL3 for local earthquakes and explosions, U. S. Geological Survey, Open File Report 94-431.

Freund, R. *et al.,* 1970. The shear along the Dead Sea Rift, *Phil. Trans. R. Soc. Lond.,* **267**(1181), 107–130.

Frieslander, U. & Ben-Avraham, Z., 1989. Magnetic field over the Dead Sea and vicinity, *Mar. Pet. Geol.,* **6,** 148–160.

Gardosh, M., Kashai, E., Salhov, S., Shulman, H. & Tannenbaum, E., 1997. Hydrocarbon exploration in the southern Dead Sea area, in *The Dead Sea: The Lake and its Setting,* Oxford Monogr. Geol. Geophys. Vol. 36, pp. 57–72, eds Niemi, T.M., Ben-Avraham, Z. & Gat, J.R., Oxford University Press, Oxford.

Garfunkel, Z., 1981. Internal structure of the Dead Sea leaky transform (rift) in relation to plate kinematics, *Tectonophysics,* **80,** 81–108.

Garfunkel, Z., 1997. The history and formation of the Dead Sea basin, in *The Dead Sea: The Lake and its Setting,* Oxford Monogr. Geol. Geophys. Vol. 36, pp. 36–56, eds Niemi, T.M., Ben-Avraham, Z. & Gat, J.R., Oxford University Press, Oxford.

Garfunkel, Z. & Ben-Avraham, Z., 1996. The structure of the Dead Sea basin, *Tectonophysics,* **266,** 155–176.

Garfunkel, Z. & Ben-Avraham, Z., 2001. Basins along the Dead Sea Transform, *Mem. Mus. Natn. Hist. Nat.,* **186,** 607–627.

Ginzburg, A. & Ben-Avraham, Z., 1997. A seismic refraction study of the north basin of the Dead Sea, Israel, *Geophys. Res. Lett.,* **24,** 2 063–2 066, doi:10.1029/97GL01884.

Haslinger, F. *et al.*, 1999. 3D crustal structure from local earthquake tomography around the Gulf of Arta (Ionian region, NW Greece), *Tectonophysics,* **304,** 201–218.

Hofstetter, A., Dorbath, C., Rybakov, M. & Goldsmidt, V., 2000. Crustal and upper mantle structure across the Dead Sea rift and Israel from teleseismic P-wave tomography and gravity data, *Tectonophysics,* **327,** 37–59.

Hofstetter, A., Dorbath, C. & Calò, M., 2012. Crustal structure of the Dead Sea basin from local earthquake tomography, *Geophys. J. Int.,* **189,** 554–568, doi:10.1111/j.1365-246X.2012.05369.x.

Hofstetter, R., Gitterman, Y., Pinsky, V., Kraeva, N. & Feldman, L., 2008. Seismological observations of the northern Dead Sea basin earthquake on 11 February 2004 and its associated activity, *Israel J. Earth Sci.,* **57,** 101–124, doi: 10.1560/IJES.57.2.101.

Husen, S., Kissling, E. & Flueh, E.R., 2000. Local earthquake tomography of shallow subduction in north Chile: a combined onshore and offshore study, *J. geophys. Res.,* **105**(B12), 28 183–28 198.

Husen, S., Smith, R.B. & Waite, G.P., 2004. Evidence for gas and magmatic sources beneath the Yellowstone volcanic field from seismic tomographic imaging, *J. Volc. Geotherm. Res.,* **131,** 397–410.

Kaypak, B., 2008. Three-dimensional Vp and Vp/Vs structure of the upper crust in the Erzincan basin (eastern Turkey), *J. geophys. Res.,* **113,** B07307, doi: 10.1029/2006JB004905.

Kissling, E., 1988. Geotomography with local earthquake data, *Rev. Geophys.,* **26**(4), 659–698.

Kissling, E., Ellsworth, W.L., Eberhardt-Phillips, D. & Kradolfer, U., 1994. Initial reference models in local earthquake tomography, *J. geophys. Res.,* **99,** 19 635–19 646.

Kissling, E., Husen, S. & Haslinger, F., 2001. Model parametrization in seismic tomography: a choice of consequence for the solution quality, *Phys. Earth planet. Inter.,* **123,** 89–101.

Klinger, Y., Avouac, J., Dorbath, L., Karaki, N.A. & Tisnerat, N., 2000. Seismic behaviour of the Dead Sea fault along Araba valley, Jordan, *Geophys. J. Int.,* **142,** 769–782.

Larsen, B.D., Ben-Avraham, Z. & Shulman, H., 2002. Fault and salt tectonics in the southern Dead Sea basin, *Tectonophysics,* **346,** 71–90.

Le Beon, M. *et al.*, 2008. Slip rate and locking depth from GPS profiles across the southern Dead Sea Transform, *J. geophys. Res.,* **113,** B11403, doi:10.1029/2007JB005280.

Le Pichon, X. *et al.*, 2001. The active Main Marmara Fault, *Earth planet. Sci. Lett.,* **192,** 595–616.

Lin, G., Shearer, P.M., Hauksson, E. & Thurber, C.H., 2007. A three-dimensional crustal seismic velocity model for southern California from a composite event method, *J. geophys. Res.,* **112,** B11306, doi:10.1029/2007JB004977.

Lodolo, E., Menichetti, M., Bartole, R., Ben-Avraham, Z., Tassone, A. & Lippai, H., 2003. Magallanes-Fagnano continental transform fault (Tierra del Fuego, southernmost South America), *Tectonics,* **22**(6), doi:10.1029/2003TC001500.

Marquis, G. & Hyndman, R.D., 1992. Geophysical support for aqueous fluids in the deep crust: seismic and electrical relationships, *Geophys. J. Int.,* **110,** 91–105.

Mechie, J., Abu-Ayyash, K., Ben-Avraham, Z., El-Kelani, R., Qabbani, I., Weber, M. & DESIRE Group, 2009. Crustal structure of the southern Dead Sea basin derived from project DESIRE wide angle seismic data, *Geophys. J. Int.,* **178,** 457–478, doi:10.1111/j.1365-246X.2009.04161.x.

Meqbel, N., Ritter, O. & DESIRE Group, 2012. A magnetotelluric transect across the Dead Sea Basin: electrical properties of geological and hydrological units of the upper crust, *Geophys. J. Int.,* submitted.

Michelini, A. & McEvilly, T.V., 1991. Seismological studies at Parkfield I: simultaneous inversion for velocity structure and hypocenters using cubic B-splines parameterization, *Bull. seism. Soc. Am.,* **81,** 524–552.

Neev, D. & Hall, J.K., 1979. Geophysical investigations in the Dead Sea, *Sediment. Geol.,* **23,** 209–238.

Paschke, M., Stiller, M., Ryberg, T., Weber, M. & DESIRE Group, 2012. The shallow P-velocity structure of the southern Dead Sea basin derived from near-vertical incidence reflection seismic data in project DESIRE, *Geophys. J. Int.,* **188,** 524–534, doi:10.1111/j.1365-246X.2011.05270.x.

Quennel, A.M., 1958. The structural and geomorphic evolution of the Dead Sea rift, *Q.J. Geol. Soc. Lond.,* **114,** 1–24.

Rahe, B., Ferrill, D.A. & Morris, A.P., 1998. Physical analog modeling of pull-apart basin evolution, *Tectonophysics,* **285,** 21–40.

Reilinger, R. *et al.*, 2006. GPS constraints on continental deformation in the Africa-Arabia-Eurasia continental collision zone and implications for the dynamics of plate interactions, *J. geophys. Res.,* **111,** B05411, doi:10.1029/2005JB004051.

Rydelek, P.A. & Sacks, I.S., 1989. Testing the completeness of earthquake catalogues and the hypothesis of self-similarity, *Nature,* **337,** 251–253.

Sagy, A., Reches, Z. & Agnon, A., 2003. Hierarchic three-dimensional structure and slip partitioning in the western Dead Sea pull-apart, *Tectonics,* **22**(1), doi:10.1029/2001TC001323.

Salamon, A., Hofstetter, A., Garfunkel, Z. & Ron, H., 2003. Seismotectonics of the Sinai subplate: the eastern Mediterranean region, *Geophys. J. Int.,* **155,** 149–173.

Shamir, G., 2006. The active structure of the Dead Sea Depression, *Geol. Soc. Am. Spec. Papers,* **401,** 15–32, doi:10.1130/2006.2401(02).

Shedlock, K.M., Brocher, T.M. & Harding, S.T., 1990. Shallow structure and deformation along the San Andreas Fault in Cholame Valley, California, based on high-resolution reflection profiling, *J. geophys. Res.,* **95**(B4), 5003–5020.

Smit, J., Brun, J.-P., Cloetingh, S. & Ben-Avraham, Z., 2010. The rift-like structure and asymmetry of the Dead Sea Fault, *Earth planet. Sci. Lett.,* **290,** 74–82.

Stern, T.A., Kleffmann, S., Okaya, D., Scherwath, M. & Bannister, S., 2001. Low seismic-wave speeds and enhanced fluid pressure beneath the Southern Alps of New Zealand, *Geology,* **29,** 679–682.

Takei, Y., 2002. Effect of pore geometry on V_P/V_S: from equilibrium geometry to crack, *J. geophys. Res.,* **107**(B2), 2043, doi:10.1029/2001JB000522.

ten Brink, U.S. & Flores, C.H., 2012. Geometry and subsidence history of the Dead Sea basin: a case for fluid-induced mid-crustal shear zone? *J. geophys. Res.,* **117,** B01406, doi:10.1029/2011JB008711.

ten Brink, U.S., Ben-Avraham, Z., Bell, R.E., Hassouneh, M., Coleman, D.F., Andreasen, G., Tibor, G. & Coakley, B., 1993. Structure of the Dead Sea pull-apart basin from gravity analyses, *J. geophys. Res.,* **98**(B12), 21 877–21 894.

ten Brink, U.S., Al Zoubi, A.S., Flores, C.H., Rotstein, Y., Qabbani, I., Harder, S.H. & Keller, G.R., 2006. Seismic imaging of deep low-velocity zone beneath the Dead Sea basin and transform fault: implications for strain localization and crustal rigidity, *Geophys. Res. Lett.,* **33,** L24314, doi:10.1029/2006GL027890.

Thurber, C.H., 1983. Earthquake locations and three-dimensional crustal structure in the Coyote Lake area, Central California, *J. geophys. Res.,* **88**(B10), 8226–8236, doi:10.1029/JB088iB10p08226.

Thurber, C.H., 1993. Local earthquake tomography: velocities and V_P/V_S-theory, in *Seismic Tomography: Theory and Practice,* Chapter 20, pp. 563–583, eds Iyer, H.M. & Hirahara, K., Chapman and Hall, London.

Toomey, D.R. & Foulger, G.R., 1989. Tomographic inversion of local earthquake data from the Hengill-Grensdalur central volcano complex, Iceland, *J. geophys. Res.,* **94**(B12), 17 497–17 510.

Um, J. & Thurber, C., 1987. A fast algorithm for two-point seismic ray tracing, *Bull. seism. Soc. Am.,* **77,** 972–986.

Uzel, B. & Sözbilir, H., 2008. A first record of a strike-slip basin in Western Anatolia and its tectonic implication: the Cumaovasi Basin, *Turkish J. Earth Sci.,* **17,** 559–591.

Wessel, P. & Smith, W. H.F., 2002. *The Generic Mapping Tools (GMT) Version 3.4.2, Technical Reference & Cookbook,* SOEST/NOAA, USA. [Available at: http://gmt.soest.hawaii.edu.]

Zak, I. & Freund, R., 1981. Asymmetry and basin migration in the Dead Sea Rift, *Tectonophysics,* **80,** 27–38.

Zhao, D., Hasegawa, A. & Horiuchi, S., 1992. Tomographic imaging of P and S wave velocity structure beneath northeastern Japan, *J. geophys. Res.,* **97** (B13), 19 909–19 928.
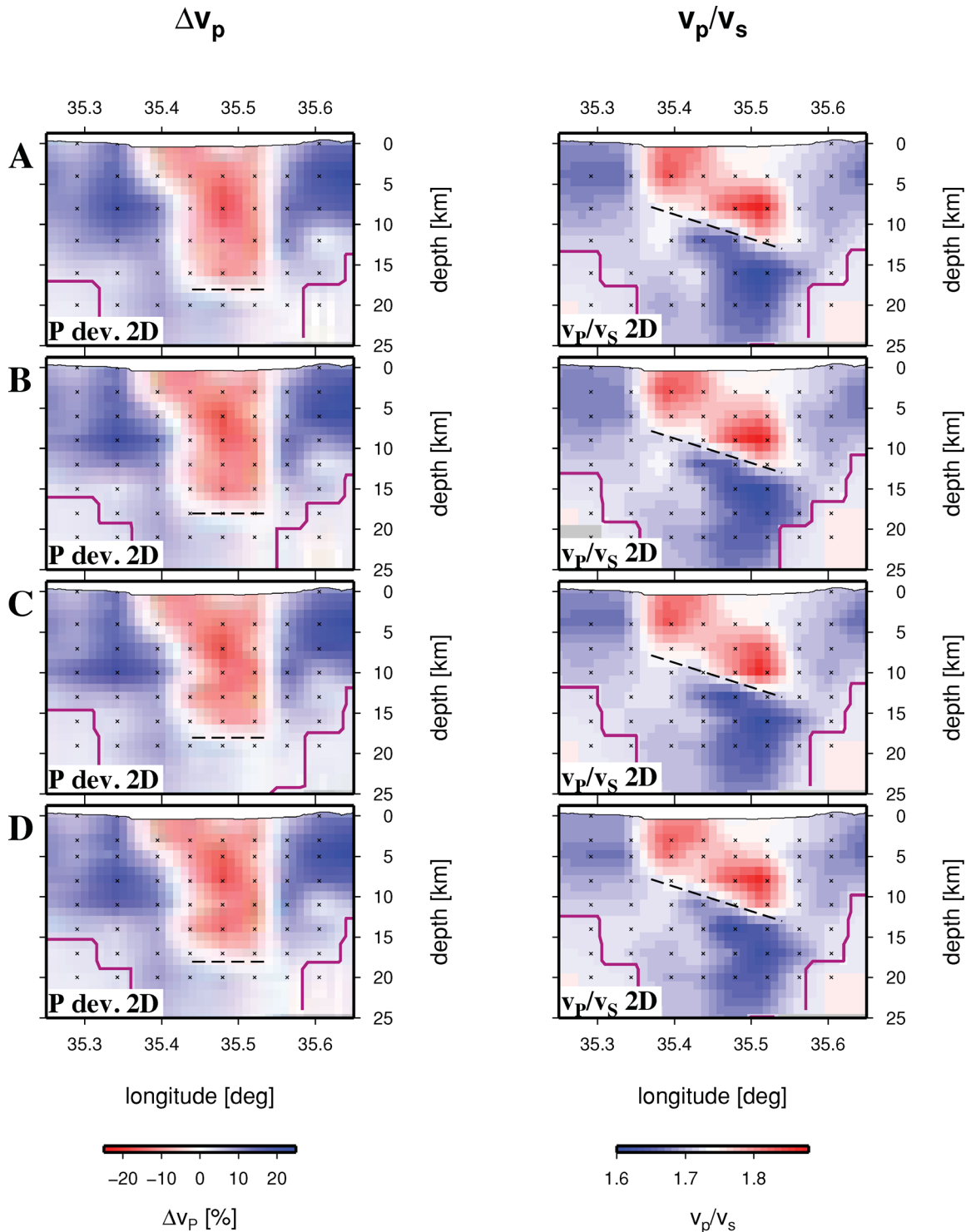
APPENDIX

Figure A1. 2-D tomographic models of v_P (left-hand side, as deviations from the background model) and v_P/v_S ratios (right-hand side) for different gridpoint distributions. (A) original gridpoint distribution with 4 km gridpoint distance in depth. (B) 3 km gridpoint distance in depth, beginning at 3 km depth. (C) 3 km gridpoint distance in depth, beginning at 4 km depth. (D) 3 km gridpoint distance in depth, beginning at 5 km depth. The lower boundary of the low P-velocity body and the high v_P/v_S body of the original model (A) is indicated in each tested model (B–D) by a dashed line, showing that these boundaries are independent of the gridpoint distribution.